Analyzing laser plasma interferograms with a continuous wavelet transform ridge extraction technique: the method

Paolo Tomassini, Antonio Giulietti, Leonida A. Gizzi, Marco Galimberti, Danilo Giulietti, Marco Borghesi, and Oswald Willi

Laser plasma interferograms are currently analyzed by extraction of the phase-shift map with fast Fourier transform (FFT) techniques [Appl. Opt. **18,** 3101 (1985)]. This methodology works well when interferograms are only marginally affected by noise and reduction of fringe visibility, but it can fail to produce accurate phase-shift maps when low-quality images are dealt with. We present a novel procedure for a phase-shift map computation that makes extensive use of the ridge extraction in the continuous wavelet transform (CWT) framework. The CWT tool is flexible because of the wide adaptability of the analyzing basis, and it can be accurate because of the intrinsic noise reduction in the ridge extraction. A comparative analysis of the accuracy performances of the new tool and the FFT-based one shows that the CWT-based tool produces phase maps considerably less noisy and that it can better resolve local inhomogeneties. © 2001 Optical Society of America

OCIS codes: 350.5400, 100.2650.

1. Introduction

Interferometric techniques are widely used to characterize the optical properties of a variety of media. An important class of application concerns the investigation of the density distribution of plasmas produced by high-intensity laser–matter interactions. In recent years various interferometer schemes have been developed and successfully applied to the characterization of the wide range of plasma conditions that can be achieved in laser plasma experiments, from the long-scale-length underdense plasma generated by laser explosion of a thin-foil target to the steep, denser plasma generated by short-pulse interaction with a solid target. All these schemes make use of a so-called probe beam that consists of a laser pulse that probes the plasma at a given time.[1,2] The fringe pattern must then be analyzed to obtain the two-dimensional phase shift that contains the physical information on the plasma. Then, provided that appropriate symmetry conditions are satisfied, inversion techniques can be applied to the phase-shift map to obtain the density profile.[3]

The traditional way of reading a fringe pattern consisted of building a grid over the pattern and measuring, for each position on the grid, the number of fringe jumps with respect to the unperturbed fringe structure. This procedure was simple and was performed manually. However, the amount of information that could be extracted in this way was limited, owing to the small number of grid points that could be employed.

In 1982 a novel fringe analysis technique was proposed[4] in which the phase extraction was carried out with a procedure based on fast Fourier transform (FFT). This technique allows the information carried by the fringe pattern to be decoupled by spatial variations in the background intensity as well as by variations in the fringe visibility, provided that the scale length of such perturbations is large compared with the fringe separation. A few years later this FFT technique was applied for the first time to laser-produced plasmas.[5] More recently the technique was extensively applied by our group to the analysis

P. Tomassini (e-mail address: tomassini@ifam.pi.cnr.it), A. Giulietti, and L. A. Gizzi are with the Intense Laser Irradiation Laboratory, Istituto di Fisica Atomica e Molecolare, Consiglio Nazionale delle Ricerche, Area della Ricerca di Pisa, Via G. Moruzzi, 1 56124 Pisa, Italy. M. Galimberti and D. Giulietti are with the Intense Laser Irradiation Laboratory, Istituto di Fisica Atomica e Molecolare, Consiglio Nazionale delle Ricerche, Dipartimento di Fisica, Università di Pisa and Istituto Nazionale per la Fisica della Materia unità di Pisa, Italy. M. Borghesi is with the Department of Pure and Applied Physics, The Queen's University, Belfast, Northern Ireland. O. Willi is with Blackett Laboratory and Imperial College, London, United Kingdom.

Received 2 April 2001; revised manuscript received 31 August 2001.

0003-6935/01/356561-08$15.00/0

of long-scale-length underdense laser plasmas.[6,7] The use of ultrashort probe pulses has considerably reduced the fringe-smearing effect caused by the motion of the plasma during the probe pulse. This fact allowed the investigation of short-lived phenomena in the propagation of ultrashort laser pulses through plasmas.[8]

The extensive use of the FFT-based technique carried out by our group has shown its effectiveness. In some circumstances, however, reduction of fringe visibility, nonuniform illumination, noise, and the presence of local image defects make the FFT-based technique unstable, and the results are not fully satisfactory because of the presence of unphysical phase jumps. In addition, small-scale nonuniformities with low departure from the density background are unlikely to be detected.

In this paper we show that continuous wavelet transforms can also be applied to the analysis of interferograms, resulting in a more flexible and reliable technique than the FFT-based one. To our knowledge, this is the first time that such an approach is applied to fringe pattern analysis.

In Section 2 we will briefly introduce the continuous wavelet transform (CWT) and its remarkable properties of a good space-scale analyzer.

In Section 3 we introduce our interferogram analysis by continuous wavelet transform ridge extraction (IACRE) tool for interferograms analysis, and we compare its sensitivity to the FFT-based method.

Section 4 is devoted to conclusions and comments.

2. Continuous Wavelet Transform Analysis Tool

The CWT is a tool to obtain a representation of signal s that is intermediate between the real-time description $s = s(t)$ and the spectral description $\hat{s} = \hat{s}(\omega)$, so that it is a powerful tool to obtain a time–frequency description of a sequence of data. In this paper the words "time" and "space" or "frequency" and "spatial frequency" will be used interchangeably.

The need for a time–frequency description of a sequence is clear when the signal represents a sum of frequency-modulated components (as for each section of an interferogram image, as shown below). This is because in a purely spectral analysis the frequency content of a modulated sinusoid is generally spread in a large region, and thus no identification of the signal from its spectral amplitude can be made.

The obvious step that can be made to overcome the lack of time sensitivity is the introduction of a sequence of windows of a given width and centered at different times: For each window the FFT of the signal is computed and a partial time resolution is obtained. These techniques are called short-time Fourier transform or Gabor transform.[9] The Gabor transform is currently used in many contexts but is not considered by the signal-processing community a full-analysis tool. This is because the number of oscillations of each sinus in the window depends on the frequency, and, consequently, the spectral and spatial resolutions can be optimized (by tuning the window length) only in a narrow band.

From the early 1980's, with the introduction of the wavelet transform, a satisfying time–frequency analysis tool was available.[10–12]

To introduce the wavelet transform, let us first define notations for the Fourier transform. For a signal $s \in L^1(\mathcal{R}) \cap L^2(\mathcal{R})$, the Fourier coefficients, that is, the scalar product between the signal and the infinitely oscillating terms $e_\omega = \exp(-i\omega t)$,

$$\hat{s}(\omega) \equiv \langle e_\omega | s \rangle = \int_{-\infty}^{\infty} \mathrm{d}t \, \exp(-i\omega t) s(t), \tag{1}$$

form a complete basis of the space to which s belongs.

Let us introduce a function $\Psi(t)$ called mother wavelet. Now, instead of decomposing the signal s as a sum of the pure oscillating terms e_ω (Fourier transform), we build a decomposition of s in terms of the base of all the translated (by parameter b) and scaled (by parameter a) Ψ's. The base of the CWT is then a two-parameter family of functions

$$\Psi_{a,b}(t) \equiv \frac{1}{a} \Psi\left[\frac{(t-b)}{a}\right]. \tag{2}$$

The choice of the mother wavelet used to build the analyzing base is quite free and must be adapted to the actual information that should be extracted from the signal.[11]

Once the base has been built, one can compute the CWT coefficients as the scalar product of the signal and $\Psi_{a,b}$:

$$W_s(a, b) \equiv \langle \Psi_{a,b} | s \rangle = \int_{-\infty}^{\infty} \mathrm{d}t \, \frac{1}{a} \overline{\Psi\left[\frac{(t-b)}{a}\right]} \, s(t). \tag{3}$$

A particular choice for the mother wavelet is the Morlet wavelet, which is largely used in studying signals with strong components of pure sinus or modulated sinusoids. The Morlet base has the form

$$\Psi(t) = \exp(i\omega_0 t) \exp[-(t/\tau)^2], \tag{4}$$

where the parameters ω_0 and τ control the peak frequency and the width of the wave, respectively. The product $\omega_0\tau$ controls the time and spectral resolution of the wavelet decomposition: A large τ corresponds to a long wave (high spectral resolution and low temporal resolution), whereas a small τ produces an event-based analysis (low spectral resolution and high temporal resolution).

We now face the problem of a numerical computation of the wavelet coefficients map $W_s(a, b)$. For a sequence of N samples s_i, $i = 1 \ldots N$ of s, the translation parameter b (which controls the central position of the wave envelope) can be sampled in a straightforward way: $b \rightarrow b_i$, $i = 1 \ldots N$. The scaling parameter a (which controls the characteristic scale of the wave) may be sampled as $a_j = 2^{-j/N_v}$, $j = 1 \ldots M$ (natural or log sampling), where N_v is the number of voices per octave parameter. Each a_j is called a voice, and, in the case $N_v = 12$, log sampling

exactly corresponds to the spectral sampling of musical tones in the tempered scale introduced by J. S. Bach.

The log sampling of CWT coefficients in the Morlet basis is quite useful when the spectral content of the signal is the main information to be extracted because it provides a good compromise between spatial resolution and spectral resolution. As the reader can easily check, the spectral resolution at each voice is proportional to the peak frequency of the voice (ω_0/a) so that the relative spectral uncertainty $\Delta f/f$ is constant along the a axes.

The real part of the CWT map shows an important feature of the CWT with the Morlet base: $\Re(W_s)$ is almost constant, apart from the thin band centered at the local signal frequency. Furthermore, the sequence

$$R_s(b) \equiv \Re(W_s)[b, a_R(b)], \tag{5}$$

where, for each b^*, $a_R(b^*)$ is the voice corresponding to a local maximum of the line-out of the absolute value CWT map taken at $b = b^*$, reproduces the input signal well itself. The sequence (or, more generally, the sequences when more complex signals are analyzed) (5) is called the ridge of the CWT map and represents the subset of the CWT map in which most of the energy is contained. Presently, the ridge detection of the CWT map plays an increasing role in signal processing,[13,14] especially in the search of nonstationary signals with a very low signal-to-noise ratio (see Ref. 15 and references therein). This is because the ridge submap captures the true input signal well even in the presence of a quite strong noise. Furthermore, ridge extraction in CWT maps of analytic signals represents a natural way to detect the local frequency evolution and, eventually, to recover phase information easily.

3. New Continuous Wavelet Transform–Based Method

A. Fast Fourier Transform–Based Method for Phase-Shift Estimation

The extraction of a phase-shift map, which is the computation for each pixel of an interferogram image of the phase shift with respect to a unperturbed wave profile, is usually performed with the help of a FFT-based method. Consider, for example, the interferogram of Fig. 1 of a laser-exploded foil target plasma.[6] Let its gray-level map be $I(z, x)$ and for each Z build the sequence $s_Z \equiv I(z = Z, x)$ (which is a horizontal line-out of the figure). The background fringe pattern would give sequences s_Z similar to pure oscillating terms plus noise and (possibly) a slowly varying background. If the departure of such a behavior is identified as a local frequency modulation of the oscillating term, then the phase shift $\delta\phi(z, x)$ can be easily computed as the difference between the perturbed phase at each x position and the corresponding phase of the background sequence. Figure 2 shows a sequence s_Z for $Z = 400$ (the middle of the frame). The behavior of s_Z can be identified as a frequency-modulated oscillation with local frequency

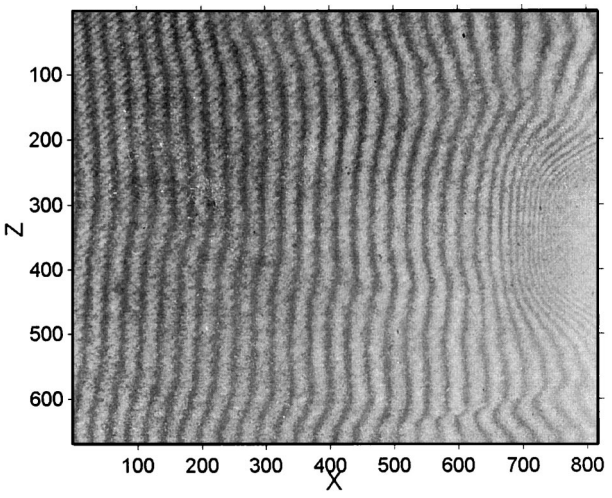

Fig. 1. Sample interferogram of a plasma produced by a laser explosion of a 0.5-μm thick, 400-μm diameter aluminium dot coated onto a 0.1-μm plastic stripe support. The interferogram was taken, perpendicularly to the strip surface, 3.0 ns after the peak of the plasma-forming pulses by use of a modified Nomarski interferometer. The intensity on target was $8.5 \times 10^{13} W/cm^2$. The probe pulse length was 100 ps, and the probe wavelength was 0.53 μm. For details on the experimental setup, see Ref. 6.

$\Omega(x)$ increasing with x, plus noise and slowly rising background. In addition, the amplitude of oscillations sharply reduces for $x \approx 700$ (this phenomenon is known as reduction of fringe visibility; see Ref. 6).

The FFT-based phase-shift extraction uses FFT for both filtering the sequence from noise and background (with cuts in the spatial-frequency domain) and extracting the phase by use of straightforward FFT coefficients manipulations.[6]

B. Phase-Shift Estimation by Interferogram Analysis by Continuous Wavelet Transform Ridge Extraction: an Introduction

To introduce the IACRE method, let us observe that the sequence s_Z [and, generally, each sequence $I(z =$

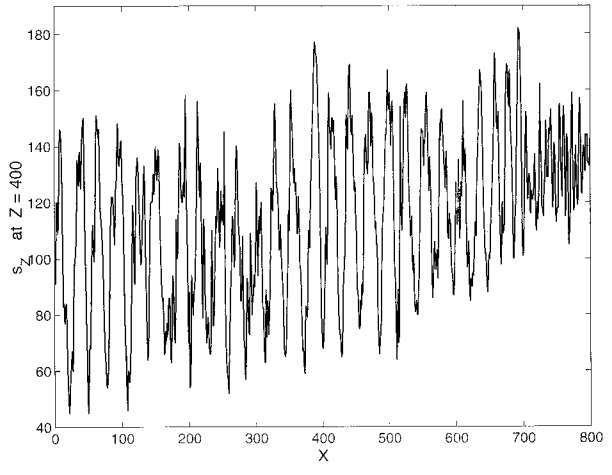

Fig. 2. Line-out of the fringe intensity (sequence s_Z) of the interferogram of Fig. 1 at $Z = 400$.

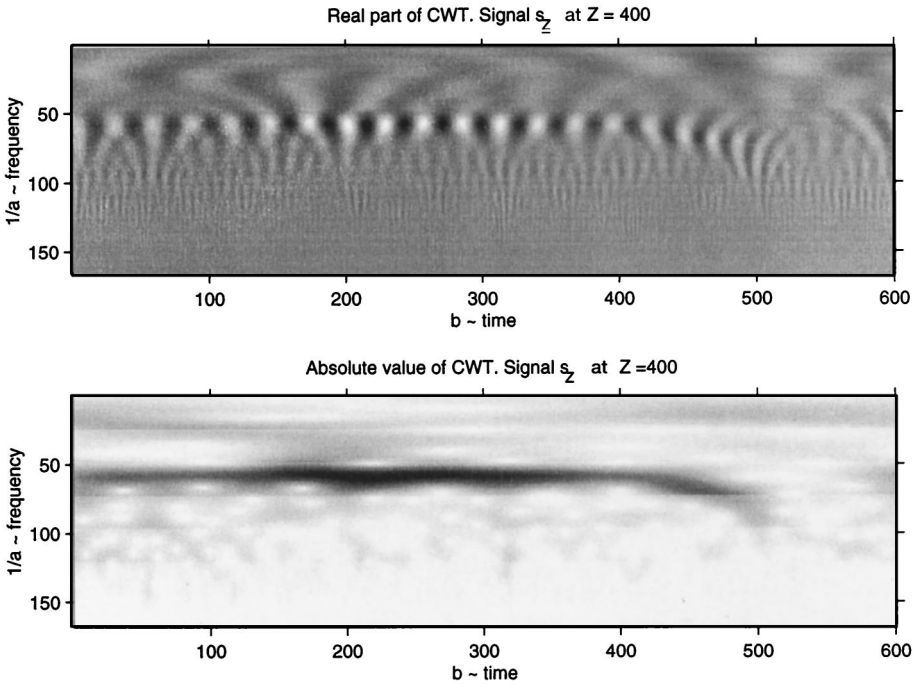

Fig. 3. Real part and absolute value of the CWT maps of the signal s_Z at $Z = 400$ (interferogram of Fig. 1).

$Z, x)]$ has the structure of a frequency-modulated sinusoid plus some corrections (noise and slowly varying background). It is therefore natural to try to extract the s_Z phase shifts by use of CWT techniques, with ridge detection playing a relevant role.

Consider the CWT map of the sequence s_Z at $Z = 400$ (see Fig. 3). We can then try to apply the ridge extraction technique to the CWT map of s_Z to both denoise the sequence and extract the phase for each pixel position x. The ridge sequence will be constituted by only the frequency-modulated components of s_Z, so that noise and background will be automatically discarded. This is the case for s_Z at $Z = 400$, as is shown in Fig. 4. The phase sequence $\phi_Z(x)$ for the analyzed array s_Z is then simply computed as the phase of the complex sequence of CWT at the ridge,

$$\phi_{s_Z}(x) \equiv \text{phase}\{(W_{sZ})[x, a_R(x)]\}, \tag{6}$$

and the phase shift $\Delta\phi_{s_Z}(x)$ is obtained as

$$\Delta\phi_{s_Z}(x) \equiv \phi_{sZ}(x) - \phi_0(x), \tag{7}$$

where $\phi_0(x) = k_p x$ and k_p is the wave number of the not-perturbed fringes.

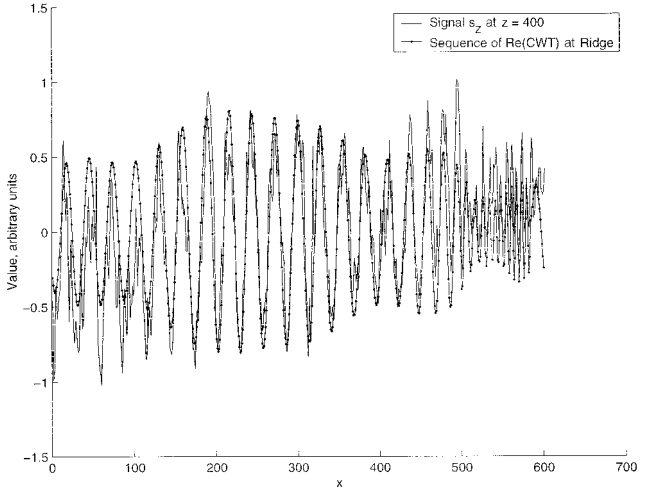

Fig. 4. Sequence of the real part of the ridge sequence of signal s_Z at $Z = 400$ (interferogram of Fig. 1).

C. IACRE Method Step by Step

Let us now examine the recipe for the IACRE algorithm. Let $I(z, x)$ be the gray-level image matrix of dimension $M \times N$. The first steps are the estimation of the unperturbed fringe wavelength k_p and (eventually) image filtering to reduce noise slightly. Next, for each $Z \in [1\ M]$ we consider the sequence

$$s_Z(x) \equiv I(z = Z, x), \qquad x \in [1N]$$

and the following.

- Compute the (complex) CWT map $W_Z(a, b)$ with the Morlet base in the log sampling. To do this, one must choose the number of voices per octave N_v. A large N_v ($N_v > 12$) should be preferred if fast changes in the local frequency $\Omega(x)$ are expected. In addition, if we expect that in some regions the local frequency $\Omega_Z(x)$ could have abrupt changes (local irregularities, structures, edges, etc.), a higher spatial resolution is preferred ($\omega_0 = 2\pi$, $\tau < 1$), whereas for regular behavior (like the one of the interferogram of Fig. 1) a medium space–frequency resolution should be used ($\tau = 1$).

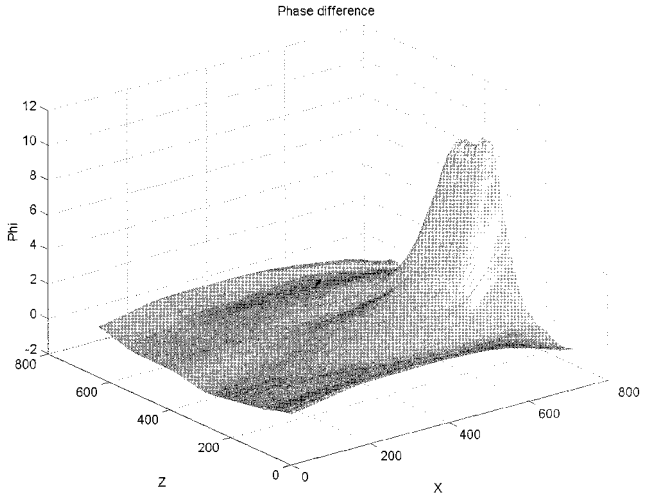

Fig. 5. Phase-shift map (in 2π units) obtained from the interferogram of Fig. 1 after suitable filtering. IACRE method.

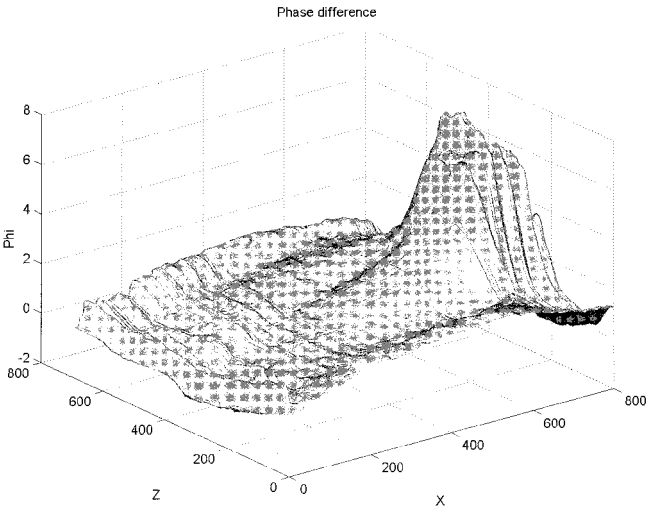

Fig. 6. Phase-shift map (in 2π units) obtained from the interferogram of Fig. 1 after suitable filtering. FFT-based method.

- Detect the (complex) ridge sequence $R_Z(x) \equiv W_{s_Z}[x, a_R(x)]$.
- Compute the phase of R_Z:

$$\phi_Z(x) = \text{phase}[R_Z(x)].$$

- Estimate the phase shift at $z = Z$ as

$$\delta\phi(Z, x) \equiv \phi_Z(x) - k_p x.$$

The result is a phase-shift matrix $\delta\phi(z, x)$ of dimension $M \times N$. Phase-unwrapping algorithms are then applied to the phase-shift map to eliminate unphysical phase jumps (this is the case for FFT-based results too).

D. Comparison between the IACRE and FFT-Based Performances

We now apply the CWT-based and FFT-based methods to both real and simulated interferogram images. To start, we apply the IACRE method to the whole interferogram of Fig. 1, which is corrupted from noise and shows a strong reduction of fringe visibility and the presence of small-scale periodical structures not related to the plasma properties.

The IACRE output result is obtained with the image partially filtered from noise with a median filter of mask size 3×3 pixels followed by a Wiener filter of 5×5 and with $N_v = 12$ voices per octave (low N_v). The phase-shift map is shown in Fig. 5, which should be compared with the FFT-method phase shift of Fig. 6 obtained with the same filtered image. As is clear from Figs. 5 and 6, although the CWT output seems to be accurate, the FFT output is noisy and is not free from unphysical phase jumps near the target, at which a strong reduction of fringe visibility is present.

The higher accuracy of the IACRE method with respect to the FFT-based one is an important characteristic of our new procedure. It permits an accurate search of small nonuniformities of the phase-shift map, which are important for detecting the growth of plasma instabilities as filamentation and self-focusing.

To better check this point, we numerically build up one interferogram in which we simulate the phase shift produced by a slowly varying background plus some small-scale filaments. Noise and reduction of fringe visibility are finally added to the interferometric image to better match the real interferograms' characteristics.

The interferogram of Fig. 7 simulates a plasma with a background of maximum electronic density $(n_e/n_c)_{\text{Max}} = 0.1$ with a Gaussian profile in the radial direction (with radius 75 μm), which is exponentially decreasing in the x direction. Three filaments are then added in different positions, each one with a Gaussian density profile,

$$\frac{\delta n(x, y, z)}{n_c} = \alpha \exp[-(z^2 + y^2)/r^2],$$

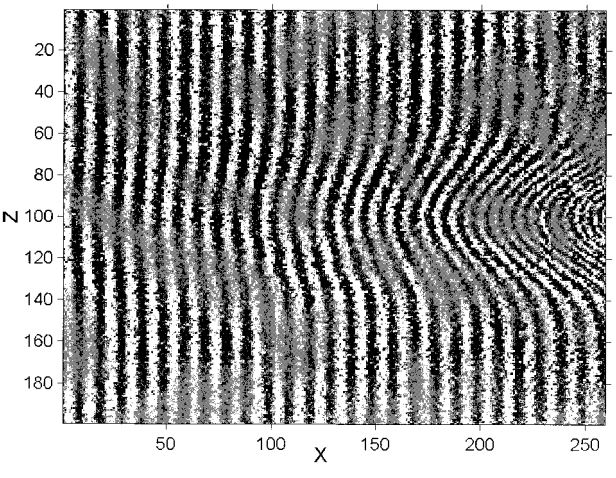

Fig. 7. Simulated interferogram of a plasma containing three small filaments.

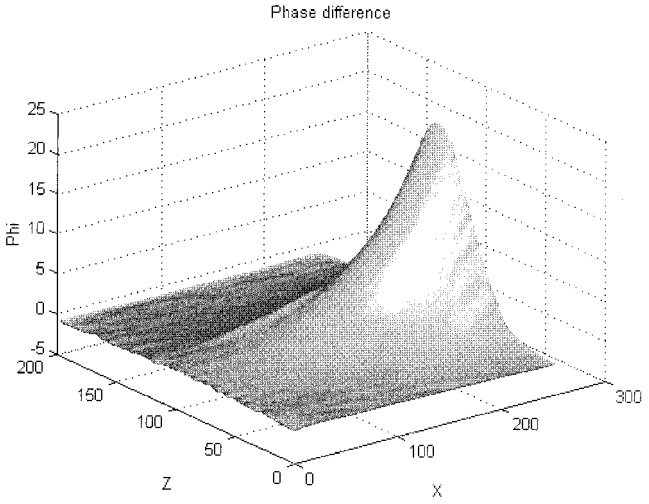

Fig. 8. Phase-shift map of the simulated interferogram of Fig. 7. IACRE method.

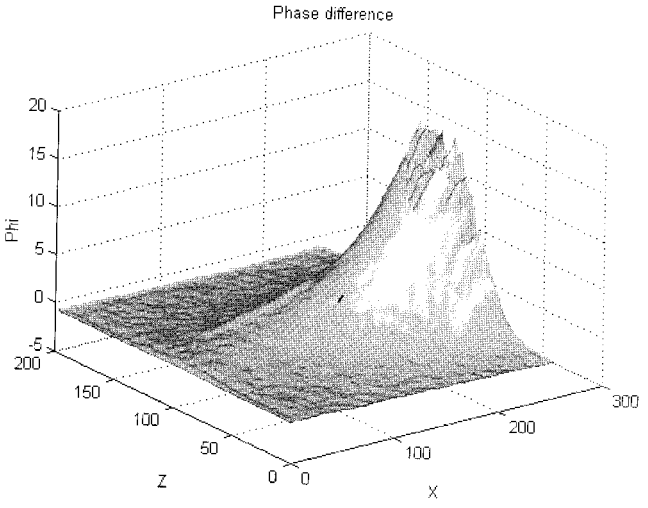

Fig. 9. Phase-shift map of the simulated interferogram of Fig. 7. FFT-based method.

with maximum density perturbation and radius ($\alpha = 0.005$, $r = 10$ μm), ($\alpha = 0.005$, $r = 8$ μm), and ($\alpha = 0.005$, $r = 6$ μm), respectively. Because the electronic density is everywhere much lower than the critical density, the linearity of the phase map with respect to the density is respected. We can then compute the perturbation of the phase-shift map in 2π units [$\phi_{2\pi} \equiv \phi/(2\pi)$] with respect to the background as

$$\delta(\Delta\phi_{2\pi}) = -\frac{1}{2\lambda_p}\int \frac{\delta n}{n_c}\,\mathrm{d}y,$$

whose maximum value is

$$\delta(\Delta\phi_{2\pi})_{\mathrm{Max}} = \frac{1}{2}\sqrt{\pi}\alpha\,\frac{r}{\lambda_p}, \tag{8}$$

where $\delta(\Delta\phi_{2\pi})_{\mathrm{Max}} = 0.18$, $\delta(\Delta\phi_{2\pi})_{\mathrm{Max}} = 0.14$, and $\delta(\Delta\phi_{2\pi})_{\mathrm{Max}} = 0.11$, respectively. To detect these structures, the noise level of the phase-shift map should be a fraction of $\delta(\Delta\phi_{2\pi})_{\mathrm{Max}}$. If $\sigma(x)$ is the standard deviation of the noise of each sequence of $\Delta\phi_{2\pi}(z, x)$ at x fixed, we could detect these structures if their amplitudes are, for instance, at two sigma with respect to the noise, $\sigma(x) < 0.09$, $\sigma(x) < 0.07$, and $\sigma(x) < 0.05$, respectively. The standard deviation $\sigma(x)$ [or one fraction of $\sigma(x)$] could then be considered a rough estimation of the detectable threshold in the phase-shift map.

To estimate the accuracy of the phase-shift maps obtained with the IACRE and FFT-based methods, we compute the phase-shift maps with the two methods (see Figs. 8 and 9), and we compare them with the known true phase map. We start the analysis by comparing some line-outs of the two phase maps with the known simulate map. In Fig. 10 it is clear that the accuracy in the two phase methods is comparable in regions of the interferogram with low phase shift, whereas for large phase shifts the FFT-based output clearly fails to produce an accurate phase map.

Denoting the phase-shifts maps obtained with the two methods as $\Delta\phi_{2\pi}^{\mathrm{CWT}}$ and $\Delta\phi_{2\pi}^{\mathrm{FFT}}$ and the simulated phase map as $\Delta\phi_{2\pi}^{\mathrm{True}}$, we estimate the error map as the differences

$$\mathscr{E}_{\mathrm{CWT}}(z, x) \equiv \Delta\phi_{2\pi}^{\mathrm{CWT}}(z, x) - \Delta\phi_{2\pi}^{\mathrm{True}}(z, x),$$
$$\mathscr{E}_{\mathrm{FFT}}(z, x) \equiv \Delta\phi_{2\pi}^{\mathrm{FFT}}(z, x) - \Delta\phi_{2\pi}^{\mathrm{True}}(z, x),$$

so that the sequences of the standard deviations of the noise in the phase map can be estimated as

$$\sigma_{\mathrm{FFT}}(x) = \mathrm{std}[\mathscr{E}_{\mathrm{FFT}}(z, x)],$$
$$\sigma_{\mathrm{CWT}}(x) = \mathrm{std}[\mathscr{E}_{\mathrm{CWT}}(z, x)], \tag{9}$$

where std[$f(z)$] is the standard deviation of the sequence $f(z)$.

Figure 11(a) shows the behavior of the error in both the IACRE and FFT-based maps and Fig. 11(b) presents the ratio $R(x)$ between $\sigma_{\mathrm{FFT}}(x)$ and $\sigma_{\mathrm{CWT}}(x)$

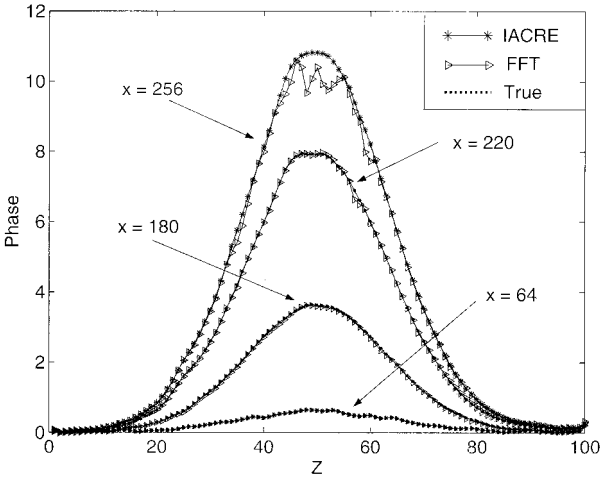

Fig. 10. Line-out of the phase-shift maps of the simulated interferogram of Fig. 7. The outputs of the IACRE and FFT-based methods are compared with the true simulated map.

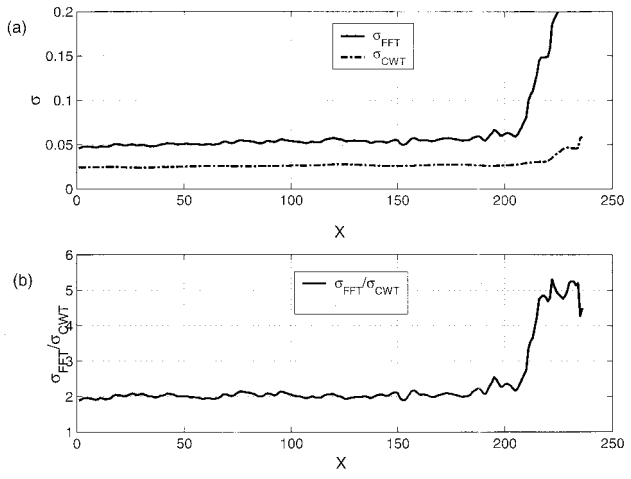

Fig. 11. (a) Standard deviations of the error in the phase-shift map of the interferogram of Fig. 7 computed via the IACRE and FFT-based methods. (b) Ratio between the standard deviations of the error in the phase-shift map of interferogram of Fig. 7 computed via the FFT-based and IACRE methods. For density perturbations δn with Gaussian density profile in the z direction of amplitude α and radius r, the sequence $\sigma_{FFT}/\sigma_{CWT}$ can also be interpreted as the ratio between the minimum product $\alpha\, r$ detectable with the FFT-based and IACRE methods: $\sigma_{FFT}/\sigma_{CWT} \sim (\alpha r)^{Min}_{FFT}/(\alpha r)^{Min}_{CWT}$.

sequences. The analysis of these figures confirms the claim that in small phase-shifts regions the IACRE method exhibits a slightly higher precision than the FFT-based one (the $\sigma_{FFT}/\sigma_{CWT}$ sequence is approximately 2), whereas in large phase-shift regions the sensibility of the IACRE method is much higher than that of the FFT-based one. For example, assuming the sequence $\sigma(x)$ is an estimation of the phase-shift sensibility, in that for Gaussian density profiles $\delta(\Delta\phi_{2\pi})_{Max}$ is proportional to the structure radius r and the maximum density perturbation α [see Eq. (8)], the sequence $R = \sigma_{FFT}/\sigma_{CWT}$ could be interpreted as a rough estimation of the ratio between the minimum product $\alpha\, r$ detectable with the FFT-based and IACRE techniques:

$$R \equiv \frac{\sigma_{FFT}}{\sigma_{CWT}} \sim \frac{(\alpha r)^{Min}_{FFT}}{(\alpha r)^{Min}_{CWT}}.$$

Furthermore, because for the IACRE method the σ_{CWT} sequence is everywhere below the value 0.03 (see the detection thresholds reported above), we are confident that all three filaments could be detected. This is not the case for the output of the FFT-based method because in the region $X \in [220,250]$ the σ_{FFT} sequence is in the range of 0.05–0.15, which is more than the minimum of the detection thresholds.

We conclude the analysis of the interferogram of Fig. 7 by checking the behavior of the phase maps when an algorithm for the automatic extraction of small-scale perturbations is applied to the phase-shift maps. The algorithm utilized is simple and consists of two main steps.

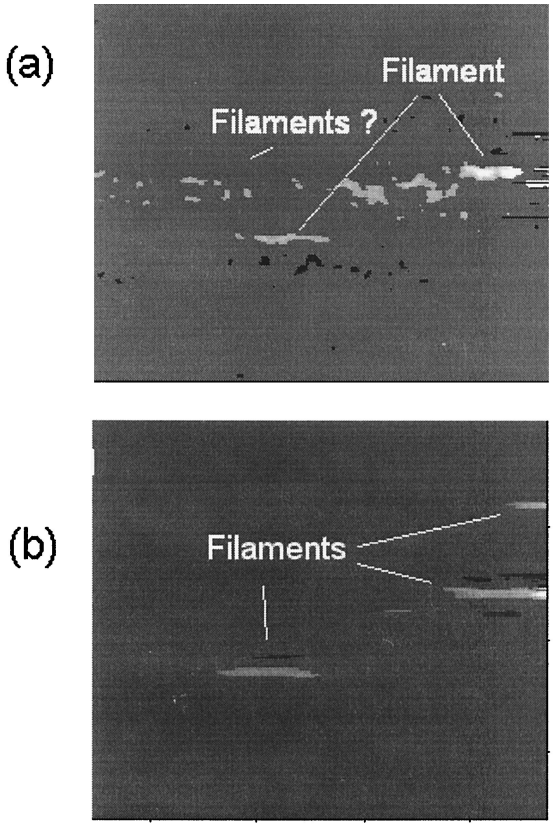

Fig. 12. Filtered map at two sigma of the small-scale component of the phase-shift map of the interferogram of Fig. 7. (a) FFT-based method: Two filaments could be detected, but other unreal structures survive to the two sigma filter. (b) IACRE method: Three filaments are clearly detected.

- The decomposition of the map $\Delta\phi_{2\pi}$ in a large-scale component (the background) $\bar{\Delta}\phi_{2\pi}$ and a small-scale component $\delta(\Delta\phi_{2\pi})$ (the structures plus noise) by use of a smoothing B-spline fitting for each line-out of the phase map at a fixed x.
- The filtering of the small-scale component $\delta(\Delta\phi_{2\pi})$ with a two sigma cutoff. As explained before, provided that structures in the $\delta(\Delta\phi_{2\pi})$ give a negligible contribution in the root-mean-square of the map, the standard deviations $\sigma_{FFT}(x)$ and $\sigma_{FFT}(x)$ can be computed as

$$\sigma_{FFT}(x) = \mathrm{std}[\delta(\Delta\phi^{FFT}_{2\pi})(z, x)],$$
$$\sigma_{CWT}(x) = \mathrm{std}[\delta(\Delta\phi^{CWT}_{2\pi})(z, x)]. \quad (10)$$

In Fig. 12 the filtered at two sigma small-scale phase maps obtained with the two methods are reported. As expected, the filtered map of the IACRE method clearly shows the presence of the three filaments, whereas in the FFT-based map some regions of the map with a strong presence of noise could be interpreted as false small-scale structures so no clear filaments detection is possible.

4. Conclusions

With the help of one real and one simulated interferograms we showed that the IACRE method is more

accurate and robust than the FFT-based one. For the simulated interferogram the smallest detectable phase-shift perturbation (with respect to the background) obtained with the IACRE method is in the mean 0.5 times the one obtained with the FFT-based one, with possible further decrease in higher-density regions. In addition the outputs of IACRE are free from unphysical phase jumps in both the real and the simulated interferograms, whereas the FFT-based map is in both cases affected by a large region near the target in which phase jumps cannot be removed by conventional unwrapping procedures. The higher robustness and sensibility of the IACRE method can be addressed to both the wide adaptability of the CWT tool to the actual image and the intrinsic strong noise suppression in the ridge extraction procedure.

The authors acknowledge support from the Italian Ministero dell' Universitá Ricerca Scientifica e Tecnologica (project: Metodologie e diagnostiche per materiali e ambiente). P. Tomassini also thanks Guido Buresti (University of Pisa) and Elena Cuoco (Istituto Nazionale di Fisica Nucleare, section of Firenze–Urbino) for useful discussions on the continuous wavelet transform.

References

1. R. Benattar, C. Popovics, and R. Siegel, "Polarized light interferometer for laser fusion studies," Rev. Sci. Instrum. **50,** 1583–1585 (1979).
2. O. Willi, "Diagnostics and experimental methods of laser produced plasmas," in *Laser-Plasma Interaction 4* of Proceedings of XXXV Scottish Universities Summer School in Physics (Scottish Universities Summer School in Physics, University of Edinburgh, Scotland, UK, 1988), pp. 213–252.
3. P. Tomassini and A. Giulietti, "A generalization of Abel inversion to nonaxisymmetric density distribution," Opt. Comm. (to be published).
4. M. Takeda, H. Ina, and S. Kobayashi, "Fourier-transform method of fringe-pattern analysis for computer-based topography and interferometry," J. Opt. Soc. Am. **72,** 156–160 (1982).
5. K. A. Nugent, "Interferogram analysis using an accurate fully automatic algorithm," Appl. Opt. **18,** 3101–3105 (1985).
6. L. A. Gizzi, D. Giulietti, A. Giulietti, T. Afshar-Rad, V. Biancalana, P. Chessa, E. Schifano, S. M. Viana, and O. Willi, "Characterisation of laser plasmas for interaction studies," Phys. Rev. E **49,** 5628–5643 (1994).
7. L. A. Gizzi, D. Giulietti, A. Giulietti, T. Afshar-Rad, V. Biancalana, P. Chessa, E. Schifano, S. M. Viana, and O. Willi, "Characterisation of laser plasmas for interaction studies. Erratum," Phys. Rev. E **50,** 4266–4267 (1994).
8. M. Borghesi, A. Giulietti, D. Giulietti, L. A. Gizzi, A. Macchi, and O. Willi, "Characterization of laser plasmas for interaction studies: progress in time-resolved density mapping," Phys. Rev. E **54,** 6769–6773 (1996).
9. D. Gabor, "Theory of communication," J. Inst. Electr. Eng. (London) **93,** 429–457 (1946).
10. J. Morlet, G. Arens, I. Fourgeau, and D. Giard, "Wave propagation and sampling theory," Geophysics **47,** 203–236 (1982).
11. M. Holschneider, *Wavelet: an Analysis Tool* (Clarendon, Oxford, 1995).
12. I. Daubechies, *Ten Lectures on Wavelets* (Society for Industrial and Applied Mathematics, Philadelphia, Pa., 1992).
13. R. Carmona, W. L. Hwang, and B. Torresani, "Characterization of signals by the ridges of their wavelet transform," IEEE Trans. Signal Process. **45,** 2586–2590 (1997).
14. B. Torresani, "Time frequency and time scale analysis," in *Signal Processing for Multimedia*, J. Byrnes, ed. (IOS, Amsterdam, 2000), pp. 37–52.
15. J. M. Innocent and B. Torresani, "A multiresolution strategy for detection gravitational waves generated by binary coalescence," submitted to Phys. Rev. D.